

Online Research @ Cardiff

This is an Open Access document downloaded from ORCA, Cardiff University's institutional repository: https://orca.cardiff.ac.uk/id/eprint/101022/

This is the author's version of a work that was submitted to / accepted for publication.

Citation for final published version:

McGrath, Deirdre, Ravikumar, Nishant, Beltrachini, Leandro ORCID: https://orcid.org/0000-0003-4602-1416, Wilkinson, Iain, Frangi, Alejandro and Taylor, Zeike 2016. Evaluation of wave delivery methodology for brain MRE: Insights from computational simulations. Magnetic Resonance in Medicine 78 (1), pp. 341-356. 10.1002/mrm.26333 filefile

Publishers page: http://dx.doi.org/10.1002/mrm.26333 http://dx.doi.org/10.1002/mrm.26333

Please note:

Changes made as a result of publishing processes such as copy-editing, formatting and page numbers may not be reflected in this version. For the definitive version of this publication, please refer to the published source. You are advised to consult the publisher's version if you wish to cite this paper.

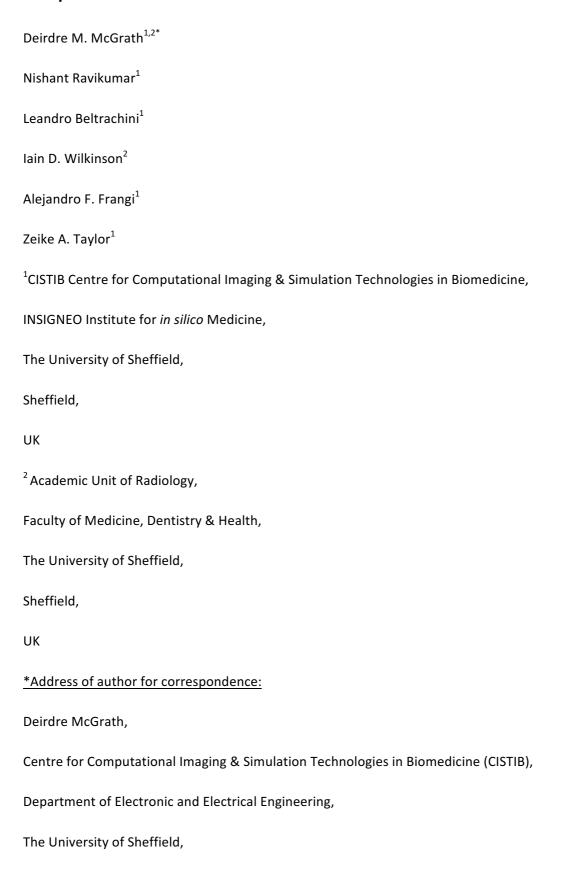
This version is being made available in accordance with publisher policies.

See

http://orca.cf.ac.uk/policies.html for usage policies. Copyright and moral rights for publications made available in ORCA are retained by the copyright holders.



Evaluation of Wave Delivery Methodology for Brain MRE: Insights from Computational Simulations



C14, Pam Liversidge Building,

Mappin Street,

Sheffield,

S1 3JD

Tel: 0114-2225398

d.mcgrath@sheffield.ac.uk

Note: A.F. Frangi and Z.A. Taylor are joint senior authors

Word count:

Running head: Simulation of cranial vibration during brain MRE to evaluate wave delivery methodologies

ABSTRACT

Purpose: Magnetic resonance elastography (MRE) of the brain is being explored as a biomarker of neurodegenerative disease such as dementia. However, MRE measures for healthy brain have varied widely. Differing wave delivery methodologies may have influenced this, hence finite element-based simulations were carried out to explore this possibility.

Methods: The natural frequencies of a series of cranial models were calculated, and MRE-associated vibration was simulated for different wave delivery methods at varying frequency. Displacement fields and the corresponding brain constitutive properties estimated by standard inversion techniques were compared across delivery methods and frequencies.

Results: The delivery methods produced widely different MRE displacement fields and inversions. Furthermore, resonances at natural frequencies influenced the displacement patterns. Two of the wave delivery methods (head-cradle and acoustic pillow) gave rise to lower inversion errors, e.g., at 90 Hz the error in the storage modulus was 11% less than for the bite-bar method.

Conclusion: Wave delivery has an important impact on brain MRE reliability. Assuming small variations in brain biomechanics, as recently reported to accompany neurodegenerative disease (e.g., 7% for Alzheimer's disease), the effect of wave delivery is important. Hence, a consensus should be established on the optimum methodology, to ensure diagnostic and prognostic consistency.

KEYWORDS: Magnetic resonance elastography; brain; skull; finite element modeling simulation; natural frequencies; dementia

INTRODUCTION

Magnetic resonance elastography (MRE) (1) is a non-invasive method for measuring the biomechanical properties of biological tissue. This is achieved by delivery of mechanical waves to the site of interest, and measurement of the resulting displacement field using MRI. Biomechanical properties, such as stiffness and viscosity, are reconstructed from the displacement field using inversion algorithms. MRE of the brain is currently being explored for the diagnosis of neurological and neurodegenerative disease such as dementia (2-11). This evaluation is complicated by the fact that the MRE measures obtained so far for healthy brain have varied widely (12-15). In a review of healthy brain MRE data (12) the shear modulus values reported for white matter varied between 2.5 and 15.2 kPa, and for grey matter between 2.8 and 12.9 kPa. Additionally, some MRE studies have reported a dependency of brain elasticity and viscosity on age and gender (16,17). Moreover, the expected influence of neurodegenerative disease on brain biomechanics is low, e.g., in (2) only a 7% decrease in shear stiffness was reported for Alzheimer's disease compared with healthy controls. While the variation in healthy brain MRE data may reflect true heterogeneity across populations, it is also possible that these measures were influenced by methodological variations between studies, such as different inversion algorithms or other post-processing steps such as filters, or the signal to noise (SNR) of the acquisitions. For instance, in (18) it was found that MRE measures for brain were strongly dependent on SNR and on the region of interest selected. Another possibility is that differences in wave delivery method methodology and excitation frequency had an influence. . MRE waves are transmitted to the brain via vibration of the skull. However, as yet little is known about the motion of the cranium during this process, which is likely to depend on the mechanism of wave delivery, the wave frequency, and the specific characteristics and inter-subject variability of the anatomy of the skull. The mode of wave delivery has varied greatly between studies, e.g., bite bar (19) mechanical head actuator (16), and acoustic pillow (2). The wave frequency has also differed; however, as brain tissue exhibits viscoelastic properties, different viscoelastic moduli values are expected for different frequencies, and some studies have sought to characterize frequencydependent effects (16,20,21).

Much previous work has been carried out using finite element model (FEM) based analysis to simulate motion of the human head during injury (22). Some studies have simulated or measured the natural frequencies (NFs) of the human skull, to predict the response of the skull to collision impact (23,24), to model the conduction of sound through the skull to aid hearing (25,26), or to understand skull vibration during surgical intervention (27). Recently, our group used steady state harmonic analysis to model MRE-associated wave propagation in the human brain to investigate the

influence of reflections and heterogeneity across boundaries of anatomical structures, i.e., the processes of the *dura mater* and the ventricles (28). It was found that this anatomy influenced the displacement fields and led to error artifacts in the inversion calculation of the brain biomechanical properties. In this earlier work, to simplify the modeling of wave delivery to the brain, the skull was not included in the model, and vibration delivery was modeled from the *pia mater* of the brain using displacement loading with a uniform direction and magnitude. However, this simplification also excludes the possibility of modeling the effects of different skull excitation approaches.

In the current study it was sought to extend our FEM simulation framework to model the vibration dynamics of the skull during MRE, and thereby to determine their dependency on the wave delivery approach and frequency. Moreover, it was sought to determine the impact of varying wave delivery at the skull on the MRE displacement field in the brain, and on the derived biomechanical properties. The hypothesis was that the method of wave delivery and wave frequency would lead to different vibration fields in the skull and therefore in the brain, which would in turn influence the estimation of the biomechanical properties of the brain. As a preliminary step, modal analysis was carried out to understand the influence of the skull's various anatomical features on its natural frequencies and associated modes of vibration. To the best of our knowledge, this is the first report addressing the modeling of vibration dynamics of the whole human head during MRE.

METHODS

Overview of FEM simulations

All simulations were carried out using Abaqus v6.12 (Dassault Systèmes Simulia Corp, Johnston, RI, USA), and details are listed in Table 1.

Modal analysis to determine natural frequencies

FEM-based natural frequency (modal) analysis was carried out on skull-only models and a full head model derived from the XCAT phantom (a data set based on imaging, defining anatomical structures of the human body at high resolution) (29). The purpose of this investigation was to gain understanding of the influence of different anatomical components on cranial vibration. Varying material properties and different boundary conditions were also compared. Furthermore, for intersubject comparison, modal analysis was carried out on a skull-only model derived from CT data.

Harmonic analysis to predict MRE wave propagation patterns

MRE wave propagation was simulated using harmonic analysis with the XCAT and CT derived models to investigate how skull vibration changes with wave delivery method and frequency. Comparison of the skull-only and full head XCAT models gives insight into the influence of the soft tissues on cranial vibration. Moreover, the full head model allows simulation of the complete propagation of vibrations from the skull to the brain, as desired, and exploration of the influence of wave delivery modes and frequency on brain displacement fields and, thereby, recovered tissue properties.

Models derived from the XCAT phantom (XM)

A set of skull models and a full head model were derived from the XCAT phantom (29) (XM1-XM6, Fig. 1). Surface meshes from the phantom were first interpolated onto a regular grid to create individual segmentations for the included anatomical structures. For the full head model, the segmentations were assigned different labels and merged to create a single multi-label segmentation. Next, a volumetric (tetrahedral) finite element mesh was generated in Matlab (R2012a, Mathworks Inc., Natick, MA) using the ISO2MESH software package (30). The volumetric mesh generation algorithm used within ISO2MESH is based on the CGAL library (CGAL, Computational Geometry Algorithms Library, cgal.org). The primary advantage of generating a volumetric mesh from a multi-label segmentation in this manner is the automatic generation of shared nodes between adjacent structures. Additionally, the ISO2MESH package provides user control over the tetrahedral element size to be applied to each region in the mesh, for computational efficiency.

The XM models included various combinations of anatomical components, to evaluate their respective influences (Fig. 1). XM1: upper skull, excluding jaw and neck; XM2: upper skull including jaw, but excluding neck; XM3: upper skull, plus jaw and neck. The upper skull contained a cavity corresponding to the sinuses. For models XM1-XM3 all bone was assigned properties as for cortical bone (see section: "Tissue material properties"). XM4: a further refined model was generated from XM3, in which extra structures were defined at the connection points of the jaw with the skull, and assigned material properties as for cartilage (two versions: Cartilage #1 and Cartilage #2 in Table 2). XM5: this model was a refinement of XM4 in which the upper skull and jaw included inner regions of cancellous bone. The cancellous bone was added using ISO2MESH by eroding the skull volume, while avoiding intersections with the sinuses. The erosion was performed until a realistic geometry for the cancellous bone was obtained, as assessed by visual comparison with the Colin 27 atlas segmentation (31).

XM6 was a refinement of XM5 in which additional regions were added: 1) brain in the inner skull cavity; 2) a layer of cerebrospinal fluid (CSF) surrounding the brain to approximate the meninges; 3)

a volume to define the ventricles inside the brain, filled with CSF; 4) the processes of the *dura mater*, the *falx cerebri* and the *tentorium and falx cerebelli* membranes (denoted "FTM"), which lie between the hemispheres of the cortex, between the cortex and the cerebellum, and between the hemispheres of the cerebellum, respectively; 5) a single volume for the tissues (skin, muscle, fat, etc.) surrounding the skull and neck; and 6) the section of spinal cord on the inside of the neck. The *meninges* and FTM were not included in the original XCAT phantom data but were added based on estimations informed by manual segmentations of other anatomical MRI data. The approximate volume of the finite elements of the brain, CSF and FTM meshes matched that of the equivalent meshes employed in (28) (i.e., $\leq 2 \text{ mm}^3$), while, for computational efficiency, the other structures were modeled with a lower element density (i.e., element volume $\leq 4 \text{ mm}^3$). As the brain and CSF regions were modeled as near incompressible material, they were meshed with hybrid (linear-pressure) elements, which discretize and solve for the pressure field independently of the displacements, to avoid volumetric locking.

Skull model derived from CT data (CTM)

To explore the generality of the findings for the XCAT skull, a second skull model was prepared. This model (CTM, Fig 2a) was generated from a probabilistic atlas derived from the computed tomography (CT) images of patients (n=33), provided in a public domain database for computational anatomy (imagenglab.com/pddca_18.html). The probabilistic atlas was used as it represents the average skull shape for a population, and hence describes a more general anatomy. Additionally, in comparison to the raw patient CT images, the atlas is less noisy and hence easier to process. The skull was segmented semi-automatically from the atlas using ITK-SNAP (32). The segmentation process involved a combination of intensity thresholding and geodesic active contour propagation to segment the skull (including the jaw) and the first three vertebrae. A volumetric mesh was subsequently generated from the skull segmentation, similarly to the preparation of the XM models. The model included the skull, jaw and neck and a gap for the sinuses, and the material properties of elastic cortical bone were employed for the whole skull (i.e., no cartilage or cancellous bone included).

Tissue material properties

All tissue constitutive properties are summarized in Table 2. Cortical bone and cancellous bone were modeled initially as linear elastic solids with properties as defined in (33). Viscous damping was later added to both, in accordance with (34). Brain was modeled as a soft homogeneous isotropic linear viscoelastic near-incompressible material, with storage (G') and loss (G") moduli values taken from MRE measurements in healthy brain at 25-90 Hz (16,19) and the density was approximated to that

of water (1,000 kg/m³) (16). The Poisson's ratio was set to 0.499999; estimated using the approximate speed of sound in the brain (1,550 ms¹). Cerebrospinal fluid (CSF) in the meninges and ventricles was modeled as a soft viscoelastic solid (33). All other tissues were modeled as linear elastic solids, with parameters taken from the following sources: cartilage Young's modulus and density were estimated from (35), and two different Poisson's ratio values (0.5 and 0.1) were assumed to explore the effect of varying the cartilage properties, and thereby influencing the range of relative movement between the jaw and skull; tissues surrounding the skull and neck (skin, muscle, fat, etc.) were modeled as a uniform volume with properties of the scalp used in (33); spinal cord was modeled as a linear elastic solid, with the elastic modulus taken from (36), with an approximated Poisson's ratio and density; and the processes of the FTM were assigned properties from (24).

Boundary conditions

Different boundary conditions (BC) were applied for the various simulations (Table 1, Fig. 1). BC1: free boundaries; BC2: for models XM1 and XM2, in which the neck was excluded, nodes near to where the neck would attach to the skull were tethered (x, y and z displacements set to zero); BC3: for models including the neck (XM3-XM6), a set of nodes at the base of the neck were tethered; BC4: for XM6 the nodes at the end of the outer tissue of the neck were also tethered to approximate the connection of the neck to the rest of the body, and to reduce the reflection of wave energy back from the end surface of the neck tissue.

Modal analysis

The natural frequencies (or eigenfrequencies) of vibration were calculated in Abaqus by eigenvalue extraction using the Lanczos eigensolver. This analysis was carried out for each XM model and material combination with varying BCs (see Table 1), and for CTM with cortical bone only and BC3. The first six NFs were compared for the models XM1-XM6 and CTM.

MRE wave propagation simulation

MRE-associated mechanical vibration at specific frequencies was simulated in Abaqus using the direct-solution steady-state dynamic analysis (hereafter referred to as harmonic analysis). This is a perturbation procedure in which the response of a model to an applied harmonic vibration is calculated about a base state, to produce frequency-space steady-state nodal displacements **u**:

$$\mathbf{u}(\mathbf{x},t) = \mathbf{u}(\mathbf{x})\exp(i\omega t) \tag{1}$$

where ω is the angular frequency, and **x** and t are spatial and temporal coordinates, respectively.

Using models XM5, XM6 and CTM, MRE simulation was carried out for frequencies at 5 Hz intervals in the range 5-150 Hz, and additionally at 37.5 and 62.5 Hz, to correspond with the frequencies included in the brain material specification (Table 2). Human brain MRE is usually carried out at <100 Hz, as brain exhibits viscoelastic behavior and strongly attenuates the MRE waves at higher frequencies, resulting in low displacement amplitudes and poor data quality. The upper limit of 150 Hz was chosen here to investigate effects in the vicinity of 100 Hz.

Displacement loading with an amplitude of 10 µm (chosen to approximate wave amplitudes observed in brain MRE) was delivered to sets of nodes at different positions on the skull surface corresponding to the different brain MRE wave delivery methods (Fig. 2): L1: "head-cradle", temples vibrated in the head-foot direction; L2: temples vibrated left-right in opposite directions; L3: temples vibrated left-right in the same direction; L4: "acoustic pillow" (2), nodes at the back of the skull vibrated in anterior-posterior direction; L5: "bite bar" (19), nodes on upper and lower jaw vibrated in left-right direction. For consistency of wave delivery between XM5 and XM6, the loading was delivered to the skull surface in XM6 rather than the outer skin surface. In the first instance, 100 nodes were selected on the skull for each loading location. To determine the sensitivity to the number of loading nodes, for 50 and 90 Hz the number of loading nodes was varied to 50 and 200 for each loading option.

The vibration fields in the skull and brain were compared for the different loading options. The viscoelastic moduli (G' and G'') were reconstructed using direct inversion (28). This algorithm was implemented in Matlab through derivative calculation using a finite difference method on a "virtual imaging voxel" grid, which was interpolated at 3 mm intervals from the FE nodal displacements. To evaluate the inversion accuracy, the mean absolute percentage difference (MAPD) was calculated for the total brain volume:

$$MAPD = \frac{100}{N} \sum_{n}^{N} \left| \frac{G_{gt} - G_{i}^{n}}{G_{gt}} \right|$$
 (2)

where N is the total number of voxels, n is the voxel number, G_{gt} the ground truth value (of G' or G'') and G_i^n the inversion value. For selection of the volume corresponding to the full brain, a 3D mask was created. The voxels at the edge of the brain are affected by various sources of error, including averaging with the surrounding tissues from interpolation, derivative calculation, smoothing of the curl vector field during inversion, errors in the direct inversion caused by tissue heterogeneity and interference patterns resulting from wave reflections at tissue boundaries (28). Hence the MAPD

was also calculated using a mask eroded by a margin of 3 voxels. By excluding this margin, understanding can be gained of the specific influence of the errors at the brain tissue edges. To explore the possible benefit of combining the results of different actuation methods, the G' and G'' voxel data was averaged for the five different loading methods, and the MAPDs calculated for the full and eroded brain volumes.

RESULTS

Natural frequencies of the XCAT skull models

The first six (non-zero) NFs of the XCAT skull models are listed in Table 3. (For all models with BC1 the first six vibration modes will always, trivially, be rigid body modes, with theoretical frequencies of 0 Hz; only frequencies for non-rigid modes, i.e., non-zero frequencies, were included in Table 3). For simulations #1-#6 (models XM1-XM3 with varying BCs) all of the first six non-zero NFs differ widely between simulations, indicating the influence of the various anatomical components and the boundary conditions. For simulation #6 (XM3, BC3) the first four NFs are 54, 82, 124 and 281 Hz. Visualization of the associated displacement fields revealed that the first three NFs are associated with the directions of rotation of the head about the neck, while the fourth NF was associated with motion of the jaw (Fig. 2g-j). For simulation #7 (XM4 with Cartilage #1, BC3) the first three NFs are unchanged, while NF#4 and subsequent NFs were altered. For simulation #8 (XM4, Cartilage #2, BC3) the first three NFs were again unchanged, while NF#4 and subsequent NFs were again altered. For XM5, with the addition of cancellous bone (simulation #9, BC3), all the NFs are slightly altered, while the first four are still associated with the same modes of vibration (Fig. 2g-j). With the addition of viscosity to the cortical and cancellous bone (simulation #10) the first six NFs are unaltered. Hence the inclusion or exclusion of the jaw and neck had a major impact on skull vibration, as did the boundary condition of tethering at the base of the neck. Based on the results of this analysis, for the MRE simulation in the skull and whole head models it was deemed necessary to include the jaw and neck and tethering at the base of the neck.

For the XM6 full head model (simulation #11, BC3+BC4), the NF calculation was strongly influenced by the soft brain tissue, and this was confirmed by visualization of the associated eigenmodes, for which various resonance patterns occurred in the soft brain tissue. Resonances occurred at intervals of approximately 1 Hz, from the minimum NF 15.4 Hz. In the MRE simulations with XM6 it was noted that resonant peaks occurred at particular frequencies associated with rotation of the head about the neck (Fig. 2g-i) (see later section: Effect of wave delivery and frequency on MRE displacement fields and inversions in XM6). It was also observed that for NFs of XM6 close to or at the resonant

frequencies for the MRE simulations of XM6, the associated eigenmodes demonstrated a strong influence of a particular direction of whole head motion about the neck, and hence the overall skull and brain displacements were larger at these NFs.

Effect of wave delivery and frequency on displacement fields in skull-only models

In Figure 3 the mean displacement components in the x, y and z directions (see Fig. 1 for the axes orientations) and the displacement vector magnitude are compared for the different MRE wave delivery methods (loading, L) and frequencies for XM5 and CTM. The plots demonstrate that resonances occur at the NFs of the models. However, for the various loading options, different resonance peaks are present or absent, depending on the direction of motion of the skull prescribed and controlled by the loading. For example, for XM5 with L1 (Fig. 3(a)), a peak occurs for the displacements in the x and y directions around 125 Hz, which corresponds to NF#3 at 127 Hz, while peaks for NF#1 and NF#2 are absent. For CTM with L1 (Fig. 3(b)), no resonance peaks are visible; however, there appears to be a gradual increase towards a peak, which would occur at the higher frequency of 230 Hz for NF#3. For XM5 with L2 (Fig.3(c)), a resonance peak occurs for the y and z components at 55 Hz, corresponding to NF#1 of 55 Hz, while for CTM (Fig. 3(d)), resonance is apparent around 115 Hz, corresponding to the NF#1 of CTM. There are similar patterns of particular resonances occurring for the other wave delivery options (L3-L5). Furthermore (far from the resonance peaks) for each wave delivery method, displacement is predominantly in a single direction (x, y or z) corresponding to the direction of loading to the skull. It is also of importance to note that the different loading methods achieve different displacement amplitudes (x, y and z) and magnitudes. For example at 37.5 Hz (far from resonance) the mean displacement magnitudes of XM5 for L1-L5 are: 20 μm; 7 μm; 9 μm; 9 μm; 7 μm. For CTM at 37.5 Hz similar mean displacements magnitudes were observed for L1-L5: 17 μm; 5 μm; 8 μm; 10 μm; 7 μm.

Figure 4 presents the displacement magnitudes plotted on the skull surface for XM5 for the various loading methods. In each case, vibration is shown at resonance, and for an example non-resonant frequency. The displacement fields differ between loading methods. Additionally, for each method, the displacement field alters greatly at resonance, when it resembles that of the corresponding eigenmode (Fig. 2g-i). Owing to the large disparity in the displacements at resonance and far from resonance, different color scales are employed in Fig. 4 for the frequencies far from resonance, and the resonant frequencies. This allows comparison between the loading methods for resonant and far from resonance frequencies withclear depiction of the displacement patterns, and allows ready comparison with the eigenmodes (Fig. 2g-i).

Effect of wave delivery and frequency on MRE displacement fields and inversions in XM6

Figure 5 presents plots of the mean displacements (x, y, z and magnitude) in the skull and brain of the XM6 model for the different loading methods and frequencies. For the skull, the displacement components again differ in magnitude, and the predominant direction varies with the wave delivery direction. Furthermore, resonance peaks whose frequencies lie within about 10 Hz of resonances for the XM5 (skull-only) model (Fig. 3) are visible. Not all the NFs of XM6 have an apparent influence on these plots, but only the NFs with eigenmodes associated with head rotation about the neck (Fig. 2g-i). These have a stronger influence on the displacement plots in Fig. 5 as the overall head displacements are higher at these frequencies. The relative proportions of the displacement components in the skull are mirrored in the displacement components of the brain, and likewise the brain resonance peaks occur in the vicinity of the resonances in the skull. Figure 5f compares the displacement magnitudes between the loading methods, revealing that for the same (10 μ m) displacement loading on the skull surface, L1 achieved the highest displacement amplitudes in the skull and brain, while L2 achieved the lowest (e.g., at 50 Hz, the mean displacement magnitude in the brain was 26 μ m for L1 and 5 μ m for L2).

Figure 6 displays the real components of the complex displacement fields, the magnitude of the curl and inversion results for a central axial brain slice of XM6 at 50 and 90 Hz. The wave patterns for the different displacement components differ widely between loading methods and frequencies. The frequencies of 50 and 90 Hz were chosen as more generally representative of the loading methods, as they lie far from the resonance peaks for all methods. They also are two of the frequencies for which G' and G" are specified for the brain material (Table 2). Loading methods L1 and L4 gave rise to similar patterns in the x, y and z displacement fields and in the inversion results, which is perhaps to be expected, as both methods result in a similar nodding motion of the head. Also, there are some similarities in the patterns observed in the z-component image slice of L1 and L4 and the 50 Hz real displacement component image in (16), where a device is employed which would result in nodding motion of the head similar to L1 and L4. Correspondingly, methods L3 and L5, which both prescribe a left-right motion of the head, also resulted in similar displacement field patterns and inversion results. For L5 at 90 Hz similar x-, y- and z-displacement patterns were observed to those presented in (19), where 90 Hz actuation is achieved via a bite-bar similar to L5. Conversely, L2 resulted in very different displacement patterns from all the other methods, though the patterns of errors in the inversion results are similar to those of L3 and L5. The magnitude of the curl of the displacement field also differs between loading options and frequencies, with generally larger curl magnitudes at the higher frequency of 90 Hz, as expected for a more rapidly varying waveform, i.e.,

a shorter wavelength. In the displayed slices, L2 and L4 had lower overall curl magnitudes compared to the other methods for both frequencies. Certain locations on the slice area tend to have larger curl magnitudes, such as either side of the falx cerebri (see last panel in Figure 1 for location of the falx cerebri in an axial slice through the brain), especially for L3 and L5. This may be associated with wave reflection off the falx, but also possible wave transmission from the falx.

Figure 7 presents plots of mean G' and G'' over the brain volume for the different wave delivery methods and frequencies, with separate error bar plots (standard deviation error bars) for the different loading methods to compare the errors between methods, and combined plots comparing the mean values for all loading methods. TheMAPD of G' and G'' for the full and eroded brain volumes, for the five frequencies of the ground truth data (Table 2) are also presented in separate error bar plots and combined plots for the five loading methods. At higher frequencies, G' varies between the methods by ~500 Pa (Fig. 7a), and G'' by ~300 Pa (Fig. 7b). To interpret the shape of the plots in Figs. 7a and 7b it is necessary to know the ground truth moduli that Abaqus employed in the simulations: for frequency-dependent viscoelastic materials, Abaqus interpolates parameters linearly within the range of specified frequencies (Table 2), and caps parameters at the bounding values outside of this range (i.e. at frequencies <25 Hz, the 25 Hz moduli are used, and at >90 Hz, the 90 Hz moduli are used). Figure 7a-b demonstrate how the variations in G' and G'' over the brain volume vary with actuation method, and the standard deviation in G' and G'' over the brain volume tends to be lower for L1 and L4 than for the other methods. The variation in G' and G'' over the brain volume also increases with frequency.

The MAPDs also vary between actuation methods, and overall L1 and L4 result in lower errors than the other methods (Fig. 7c-d) e.g., at 90 Hz, MAPD of G' for L1 and L4 was approximately 11% less than for L3 and L5, while for G" at 37.5 Hz, it was approximately 17% lower for L1 and L4 compared with L3.. For the eroded volume, the MAPDs are vastly reduced, though L1 and L4 still have predominantly the lower error values, except at the higher frequencies (62.5 and 90 Hz). However, the differences between delivery methods for the eroded mask are only on the order of 1%. The MAPDs also vary with frequency. For the full brain volume the errors on G' tend to be higher for the two extremes of 25 and 90 Hz (and the standard deviation of the error is also larger) compared to the other frequencies, while for G" the opposite holds, i.e., 25 and 90 Hz have lower errors (and standard deviations of the error). For the eroded brain volume (Fig. 7e-f) all the errors are reduced substantially compared with the full volume, and the errors and standard deviations of the errors are higher for 25 and 90 Hz for both G' and G".

Figure 7g presents error bar plots for the MAPD of the voxel-wise average G' and G" for all five loading methods, for the full and eroded brain volumes. Averaging was found to lead to marginal reductions of 1-2 % in the lowest MAPD values for G' for the full brain volumes for frequencies 25, 37.5, 50 and 62.5 Hz, while it did not achieve lower errors for 90 Hz, i.e., a 29% error compared to the lowest error at 90 Hz of 25% for L4 (Fig.7c). For the eroded brain volume for each frequency the differences between the lowest MAPDs of G' and the MAPD of the average G' were generally <1%. However for G" averaging increased the errors substantially for the full and eroded brain volumes for all five frequencies, e.g., for the full brain volume, while the maximum error for the non-averaged G" was 76% at 37.5 Hz for L3 (Fig.7d) the error at 37.5 Hz for the averaged G" was 85%. The average error (over the frequencies) of the eroded volume for the averaged G" was 52% (the minimum error of 22% was at 90 Hz, Fig. 7g), while the errors for the non-averaged G" for the eroded volume were all < 7 % (Fig.7f). Furthermore, averaging of the G' and G" voxel values tended to reduce the standard deviation of the MAPD over the brain volume for the full and eroded masks. With regard to testing the sensitivity to the number of loading nodes, it was found that for most of the wave delivery methods that changing the number of nodes only led to minor variations in the displacement fields and the inversion maps of G' and G", with the exception of L2. The MAPD of G' and G" generally varied by less than 1% between 50, 100 and 200 nodes for loading for L1, L3, L4 and L5. However for L2 the MAPDs varied more substantially. For L2 at 50 Hz with 50, 100, and 200 nodes, the MAPD of G' was 18±23%, 17±21% and 16±19% respectively, while for the MAPD of G" the values were 74±110%, 70±101%, and 66±90%. Hence, the MAPD and the standard deviation of the MAPD decreased with increasing loading nodes, however the reductions in error were more pronounced for G". For 90 Hz a similar effect was observed: with 50, 100, and 200 nodes, the MAPD of G' was 35±37%, 30±30% and 28±26% respectively, while for the MAPD of G" the values were $63\pm67\%$, $62\pm64\%$, and $62\pm62\%$. However for 90 Hz the reductions in G' were more pronounced than those of G". The variations in inversion errors for L2 appears to be mainly associated with variations in the directions and amplitudes of the displacement field, and different wave interactions at the borders of the brain tissue, leading to different reflection and interference effects. While for the other loading methods the direction of the waves was relatively unaltered by the changing number of loading nodes. That the variations are mainly at the brain tissue borders is supported by the fact that for the eroded brain volume the MAPDs and standard deviation of the MAPD varied by less than 1% for L2.

DISCUSSION

Natural frequencies of XCAT and CTM skull models

The NF analysis of the skull models XM1-XM5 revealed important information on the influence of the various anatomical components on skull vibration. As the delivery of MRE waves to the brain is mainly achieved via transmission through the skull, it is important to determine the relevant NFs of the skull (i.e., those that lie in the typical frequency range for brain MRE: 20-100 Hz), and to understand the factors that influence the eigenmodes. The inclusion of the jaw and neck, and tethering at the base of the neck strongly influenced the vibration of the skull and the NFs.

The NFs differed between CTM and the matching XM3 model (simulations #6 and #12, Table 3). The material specifications were identical for these simulations, however the volume (and therefore mass) of CTM was lower than that of XM3. NFs typically scale inversely with the square root of the mass, and hence the NFs for CTM are higher than those for XM3. However, structural variation between the models will also influence modal dynamics. While the NFs vary between models, the modes of vibration for the first four NFs are the same for both models (Fig. 2g-j).

Previous investigators have sought to measure or simulate the vibration and NFs of the human skull. However the methodology has varied widely between studies: some simulations or measurements excluded the jaw (24) or the neck (27), or both (23), and while some measurements were carried out in dry skull models (27), others were made in live human subjects (25), or both (37,38), and therefore the reported NFs have also varied widely between studies. In (24) two FE skull models were compared: one excluding the jaw and neck, and the other excluding the jaw but including the neck. Tethering was also included at the base of the skull or neck. In (24) the range of the first four NFs for the model without the neck was 149.1-860.2 Hz, while the range of the first four NFs of the nearest corresponding model in this study (XM1 with BC2) was 321-1488 Hz. As in the present study, in (24) it was found that when the neck was included the NFs were reduced (first four: 88.9-399.4 Hz), and furthermore the rotational motion of the skull for the first three modes was similar to those observed in this study (Fig. 2g-j), while the fourth was associated with head-foot motion of the skull. However, in (24) they did not include the jaw bone, whereas in the present study it was found that the fourth NF was associated with jaw motion. Moreover, in this study for BC3, NF#4 was > 200 Hz for XM3 and > 400 Hz for CTM; as brain MRE is typically carried out at < 100 Hz, this suggests that jaw motion may have a smaller influence on the motion of the skull during MRE.

In this study the NFs of the full head model (XM6) were very different to those of the skull-only model (XM5). The XM6 modal analysis was strongly influenced by the soft brain tissue, and the different anatomical structures within the cranium, and NFs occurred at intervals of approximately 1

Hz, from the minimum NF of 15.4 Hz. This differed greatly from reported NFs for *in vivo* human head: Hakansson et al. (25) measured NFs in the range 500-7,500 Hz for *in vivo* human skulls and found 14-19 resonances, with the average of the two lowest frequencies at 972 Hz. Cai et al. (37) also made *in vivo* measurements in the range 2-52 kHz and made a comparison with dry skulls. They found complex resonances and antiresonances in both the dry skulls and live head, which were strongly dependent on the transducer position, and found that damping in the live head reduced the resonance peaks.

The effect of damping from soft tissues could be observed in the MRE simulation with XM6, as the resonance peaks were shifted with respect to the XM5 skull-only model (Figs. 3 and 5). Furthermore, the MRE simulation could explore the effect of delivering wave energy at different positions, and the associated vibration effects of each delivery mode. Hence, for XM6 the MRE simulations were more informative than the modal analysis.

Inter-subject differences in skull NFs and possible implications for MRE

The different NFs of the XM3 and CTM models indicate that the NFs will change between individuals depending on the size and shape of the skull. The different resonance effects in the MRE simulations of XM5 and XM6 also indicate how NFs will shift due to the damping effects of the tissues in the head, and this is likely to vary between individuals. According to the in vivo measurements of (25,37), the NFs of the *in vivo* human head are likely to occur at > 500 Hz, which is well outside the typical frequencies employed for brain MRE, i.e., 20-100 Hz. However, the simulations in this study have demonstrated that when resonances do occur at or in the vicinity of the MRE excitation frequency they can have a major impact on the wave fields in the brain. Hence, it is the recommendation of this study that further exploration should be carried out with volunteers to determine the resonances of the human head and the impact of these on the MRE measurements. If actuation is carried out at a resonance frequency, there is the possibility of persistent nodes and anti-nodes occurring in the brain tissue, which may lead to errors in the inversions. As the MRE simulations of this study calculated the harmonic steady state displacements, it was not possible to observe the occurrence of persistent nodes, and, moreover, the errors in the inversions of this study appeared mainly related to the effects at the boundaries of brain tissue with other anatomy. However in the natural frequency simulations with the full head model XM6, symmetric displacement patterns were observed in the brain tissue that would suggest the likelihood of persistent nodes occurring in real acquisitions. This is therefore an important avenue for future investigation via MRE acquisition.

Implications of the choice of wave delivery method and frequency in brain MRE

The results of this study have proven the hypothesis that, in the context of simulation, MRE wave delivery methodology and frequency affect the displacement fields in the skull and brain, and also the inversion accuracy. Different displacement components were dominant for the different methods, while some methods had similar patterns of displacement and inversion error, i.e., L1 was similar to L4, and L3 was similar to L5. Furthermore, if the NFs lie at or close to the MRE wave frequency, a resonance peak can occur in the MRE displacement fields. Also, only particular NF resonances occur for the different loading methods, and the peaks can accentuate the differences between displacement components. For accurate inversion it is important to have balance between the displacement components in order to achieve full rank in the system of equations solved in the direct inversion (39). Hence, large disparities between displacement components caused by a particular wave delivery or resonances may lead to inaccurate inversion. However, as brain MRE studies have not reported such a large disparity between displacement components, this potential effect of resonance, or indeed the particular direction of wave delivery, appears unlikely to occur in reality, and the many approximations involved in these simulations may account for these effects. However it is a recommendation of this study that future MRE studies should investigate the possible influences of resonances or the preferential direction of waves due to the delivery method, and verify the balance of displacement components.

Overall L1 (head-cradle) and L4 (acoustic pillow) produced the lowest errors in the inversions. In Fig. 6, the inversion errors appear to be mainly associated with interaction of the wave field with the *falx cerebri* membrane, as large inversion errors occur at either side of this structure. For methods L1 and L4 the displacement field is moving predominantly in a direction parallel to the *falx* (y-direction), while for the other methods the dominant motion is left-right (x-direction), and lesser artifacts occur for L1 and L4 (especially at 50 Hz, Fig. 6). In our previous brain MRE simulation work (28) it was found that inversion artifacts occurred close to interfaces between brain tissue and the FTM and ventricles. The conclusion of that earlier study was that errors at the boundaries were caused by a combination of factors: 1) reflection, refraction and scattering at tissue boundaries leading to wave interference, which results in inversion artifacts at larger sampling steps (3 mm); 2) material heterogeneity bringing about errors in the direct inversion algorithm (which assumes local homogeneity (39)); 3) averaging across the tissue boundaries due to interpolation, derivative calculations and smoothing of the curl vector field during the inversion (28). However, the findings of this present study emphasize the importance of wave reflection and the resulting interference patterns, as the different wave delivery methods produce different predominant directions of

motion accompanied by different magnitudes of inversion error. Some sensitivity to the number of loading nodes was also observed, and particularly for L2. Based on these observations, in real MRE acquisitions it would be important to determine the sensitivity to the area of contact and positioning of the actuator, and perhaps carry out optimization of these factors.

Averaging of the G' and G'' data over the five actuation methods demonstrated only a minor benefit to the accuracy of G', and was detrimental to the accuracy of G''. However as the simulations of this study were simplified in many aspects, averaging over multiple actuation methods may prove more beneficial in real MRE acquisitions, and comparison of different actuation methods will inform assessment of the stability and reliability of measurements. In fact recent work has addressed this in the comparison of the method of (16) with a new remote actuation method for brain MRE (40). Acquisition via multiple actuation methods may be facilitated by newer faster MRE sequences (41,42).

Limitations of the current study and future work

The major limitation of this study was the simplicity of the models employed, in terms of anatomy and material specifications. The approximations involved in the FE modeling and simulations were further limitations. For instance, the anatomical models employed were based on the anatomy of a single individual (XM) and on the average model of a small cohort (CTM), and therefore do not capture all the variability of anatomy across the population. Skull shape is likely to vary with factors such gender, age and race. Future work will investigate the variability of resonant frequencies across the population by means of statistical shape modeling of the skull based on a wider population of data. The models were also simplified in terms of the structures included and the material models used, such as a soft viscoelastic solid for CSF as opposed to a fluid. Furthermore, the meninges have in reality a complex structure: the dura mater (attached to the skull) is connected to the pia mater (attached to the brain) via filaments called trabeculae running through the subarachnoid space, which is permeated with CSF. The brain is also tethered to the skull at the brain stem and via other vascular and neural connections. Furthermore, in reality slippage occurs between the skull and brain, and the meninges are likely to have non-linear material properties, and these factors have not been accounted for in the models. Given the findings of MRI spin tagging motion tracking of the brain during impact (43), the motion of the brain within the skull during MRE is likely to be very complex, with displacement, deformation and rotational motion occurring to varying degrees at different locations at the brain-skull boundary. Another study measuring MRE wave transmission from the skull to brain (44) concluded that the meninges strongly attenuate MRE waves. Furthermore, other anatomical features in the head that were not included are likely to cause wave attenuation through

viscosity and scattering at tissue interfaces, and indeed brain tissue itself is in reality heterogeneous (20), meaning waves are likely to be scattered at the interfaces of different brain regions (45). Based on the degree of wave and motion damping measured in (43,44) the degree of damping of the resonance peaks for the XM6 model (Fig.5) is likely to be underestimated. Furthermore, brain tissue is anisotropic, as the white matter is fibrous (46), and this would influence MRE displacement fields. Brain tissue is likely to be under anisotropic pre-stress, which will affect estimates of material parameters obtained using the different wave delivery locations and directions. Indeed recent work has found that the MRE measures for brain white matter differed depending on whether waves were delivered in the anterior-posterior direction or the left-right direction (47). Therefore the interaction of waves with the anisotropic structures of the brain may account for the variability in measures obtained from different brain MRE studies employing varying actuation methods, as opposed to differences in the overall displacement fields and wave interactions at the brain boundaries, or differences in inversion methods employed or other post-processing steps. Future studies will explore the sensitivity of the findings of this work to variations in material properties of the different anatomical structures.

However, the variability that might occur between individuals and the approximations employed in the material modeling do not negate the overall findings of this work, i.e., that the choice of wave delivery methodology can influence brain MRE data. Rather, studies with wider populations and varied properties would provide a better estimate of the actual impact of using different wave delivery methods.

Although further simulations are warranted to explore the limitations of the findings of this study, ultimately *in vivo* MRE studies are required to determine the actual impact on varying wave delivery. Hence, the main recommendation from this work is that volunteer studies comparing MRE acquisitions with different wave delivery methods be undertaken. In fact, in the recent study by Fehlner at al. (40) athe actuation method of (16) wascompared with a newer remote excitation method, and it was found that the magnitude and phase of the complex shear modulus could differ by as much as 6 and 13% respectively in the brain regions examined. Further similar studies should be carried out to determine a consensus methodology for optimum accuracy and stability, although patient comfort and the practicality of the method are other primary considerations.

CONCLUSIONS

Through simulation, this study has demonstrated that in brain MRE the method of wave delivery and wave frequency strongly influence the displacement fields in the skull and brain, and consequently

the accuracy of the inversion reconstructions of the brain biomechanical properties (e.g., at 90 Hz an 11% lower inversion error for the head-cradle (L1) and acoustic-pillow (L4) compared with the bite bar (L5)). However, most of these differences are associated with brain tissue located at the boundaries with other anatomy, and it is uncertain how much of the inversion error in these locations is associated with the inversion method or other sources of error from the simulation, and future work should employ other inversion methods for comparison. But given that the inversion errors at the brain boundaries differed strongly between the loading methods, it is likely that these errors are associated with different reflection, scattering and interference effects, and destructive interference and standing waves from interference pose very difficult challenges for inversion. Furthermore, the natural frequencies of vibration of the head could influence the MRE displacement fields in the brain and therefore the inversion accuracy, through the occurrence of standing waves with persistent nodes and anti-nodes, or an imbalance in displacement components at resonance.

As the models employed in this study were generated from a limited representation of human head anatomy and were simplified in various aspects, future simulation studies are required to explore the limitations of these findings. Furthermore, it is recommended that *in vivo* MRE studies are made on volunteers using the various wave delivery methods and varying frequencies, to determine the stability of the measures of brain tissue biomechanics, and the possible influence of resonant frequencies.

ACKNOWLEDGEMENTS

This study was funded by the European Union's Seventh Framework Programme (FP7/2007 – 2013) as part of the project VPH-DARE@IT (grant agreement no. 601055). There are no conflicts of interest associated with this work.

REFERENCES

- 1. Muthupuillai R, Lomas DJ, Rossman PJ, Greenleaf JF, Manduca A, Ehman RL. Magnetic resonance elastography by direct visualization of propagating acoustic strain waves. Science 1995;269(5232):1854-1857.
- 2. Murphy MC, Huston JI, Jack CRJ, Glaser KJ, Manduca A, Felmlee JP, Ehman RL. Decreased brain stiffness in Alzheimer's disease determined by magnetic resonance elastography. J Magn Reson Im 2011;34:494-498.
- 3. Wuerfel J, Paul F, Beierbach B, Hamhaber U, Klatt D, Papazoglou S, Zipp F, Martus P, Braun J, Sack I. MR-elastography reveals degradation of tissue integrity in multiple sclerosis. Neuroimage 2010;49:2520-2525.
- 4. Schregel K, Wuerfel E, Garteiser P, Gemeinhardt I, Prozorovski T, Aktas O, Merz H, Petersen D, Wuerfel J, Sinkus R. Demyelination reduces brain parenchymal stiffness quantified in vivo by magnetic resonance elastography. P NATL ACAD SCI USA 2012;109(17):6650-6655.
- 5. Murphy MC, Curran GL, Glaser KJ, Rossman PJ, Huston JI, Poduslo JF, Jack CRJ, Felmlee JP, Ehman RL. Magnetic resonance elastography of the brain in a mouse model of Alzheimer's disease: initial results. Magn Reson Imaging 2012;30:535-539.
- 6. Streitberger KJ, Sack I, Krefting D, Pfuller C, Braun J, Paul F, Wuerfel J. Brain viscoelasticity alteration in chronic-progressive multiple sclerosis. PLoS One 2012;7(1):e29888.
- 7. Freimann FB, Streitberger KJ, Klatt D, Lin K, McLaughlin J, Braun J, Sprung C, Sack I. Alteration of brain viscoelasticity after shunt treatment in normal pressure hydrocephalus. Neuroradiology 2012;54(3):189-196.
- 8. Streitberger KJ, Wiener E, Hoffmann J, Freimann FB, Klatt D, Braun J, Lin K, McLaughlin J, Sprung C, Klingebiel R, Sack I. In vivo viscoelastic properties of the brain in normal pressure hydrocephalus. NMR Biomed 2011;24(4):385-392.
- 9. Lipp A, Trbojevic R, Paul F, Fehlner A, Hirsch S, Scheel M, Noack C, Braun J, Sack I. Cerebral magnetic resonance elastography in supranuclear palsy and idiopathic Parkinson's disease. Neuroimage Clin 2013;3:381-387.
- 10. Riek K, Millward JM, Hamann I, Mueller S, Pfueller CF, Paul F, Braun J, Infante-Duarte C, Sack I. Magnetic resonance elastography reveals altered brain viscoelasticity in experimental autoimmune encephalomyelitis. Neuroimage Clin 2012;1(1):81-90.
- 11. Huston J, 3rd, Murphy MC, Boeve BF, Fattahi N, Arani A, Glaser KJ, Manduca A, Jones DT, Ehman RL. Magnetic resonance elastography of frontotemporal dementia. J Magn Reson Imaging 2015.
- 12. Di leva A, Grizzi F, Rognone E, Tse ZT, Parittotokkaporn T, Rodriguez YBF, Tschabitscher M, Matula C, Trattnig S, Rodriguez YBR. Magnetic resonance elastography: a general overview of its current and future applications in brain imaging. Neurosurg Rev 2010;33(2):137-145; .
- 13. Glaser KJ, Manduca A, Ehman RL. Review of MR elastography applications and recent developments. J Magn Reson Im 2012;36(4):757-774.
- 14. Kruse SA, Rose GH, Glaser KJ, Manduca A, Felmlee JP, Jack CR, Jr., Ehman RL. Magnetic resonance elastography of the brain. Neuroimage 2008;39(1):231-237.
- 15. Chatelin S, Constantinesco A, Willinger R. Fifty years of brain tissue mechanical testing: from in vitro to in vivo investigations. Biorheology 2010;47(5-6):255-276.
- 16. Sack I, Beierbach B, Wuerfel J, Klatt D, Hamhaber U, Papazoglou S, Martus P, Braun J. The impact of aging and gender on brain viscoelasticity. Neuroimage 2009;46(3):652-657.
- 17. Arani A, Murphy MC, Glaser KJ, Manduca A, Lake DS, Kruse SA, Jack CRJ, Ehman RL, Huston JI. Measuring the effects of aging and sex on regional brain stiffness with MR elastography in healthy older adults. Neuroimage 2015;111:59-64.
- 18. Murphy MC, Huston J, 3rd, Jack CR, Jr., Glaser KJ, Senjem ML, Chen J, Manduca A, Felmlee JP, Ehman RL. Measuring the characteristic topography of brain stiffness with magnetic resonance elastography. PLoS One 2013;8(12):e81668.

- 19. Green MA, Bilston LE, Sinkus R. In vivo brain viscoelastic properties measured by magnetic resonance elastography. NMR Biomed 2008;21(7):755-764.
- 20. Guo J, Hirsch S, Fehlner A, Papazoglou S, Scheel M, Braun J, Sack I. Towards an elastographic atlas of brain anatomy. PLoS One 2013;8(8):e71807.
- 21. Dittmann F, Hirsch S, Tzschätzsch H, Guo J, Braun J, Sack I. In vivo wideband multifrequency MR elastography of the human brain and liver. Magn Reson Med 2015:Epub 10.1002/mrm.26006.
- Tse KM, Lim SP, Tan VBC, Lee HP. A review of head injury and finite element head models. American Journal of Engineering, Technology and Society 2014;1(5):28-52.
- 23. Nickell RE, Marcal PV. In-vacuo modal dynamic response of the human head. J Eng Ind T ASME 1974;96(2):490-494
- 24. Huang BW, Ou Y-W, Chang CH, Chen GS, Yen KY, Tseng J-G. Dynamic characteristics of the skull with the neck effect. Life Sci J 2013;10(2):265-270.
- 25. Hakansson B, Brandt A, Carlsson P, Tjellstrom A. Resonance frequencies of the human skull in vivo. J Acoust Soc Am 1994;95(3):1474-1481.
- 26. Kim N, Chang Y, Stenfelt S. A three-dimensional finite-element model of a human dry skull for bone-conduction hearing. Biomed Res Int 2014;2014:519429.
- 27. Huang BW, Kung HK, Chang K-Y, Hsu PK, Tseng J-G. Human Cranium Dynamic Analysis. Life Sci J 2009;6(4):15-22.
- 28. McGrath DM, Ravikumar N, Wilkinson ID, Frangi AF, Taylor Z. Magnetic resonance elastography of the brain: An in silico study to determine the influence of cranial anatomy. Magn Reson Med 2015;doi: 10.1002/mrm.25881.
- 29. Segars WP, Sturgeon G, Mendonca S, Grimes J, Tsui BM. 4D XCAT phantom for multimodality imaging research. Med Phys 2010;37(9):4902-4915.
- 30. Fang Q, Boas D. Tetrahedral mesh generation from volumetric binary and gray-scale images. Proc IEEE Int Symp Biomed Imaging 2009:1142-1145.
- 31. Aubert-Broche B, Evans AC, Collins L. A new improved version of the realistic digital brain phantom. Neuroimage 2006;32(1):138-145.
- 32. Yushkevich PA, Piven J, Hazlett HC, Smith RG, Ho S, Gee JC, Gerig G. User-guided 3D active contour segmentation of anatomical structures: significantly improved efficiency and reliability. Neuroimage 2006;31(3):1116-1128.
- 33. Yang J. Investigation of brain trauma biomechanics in vehicle traffic accidents using human body computational models. A Wittek et al (eds), Computational biomechanics for medicine: Soft tissues and the musculoskeletal system, Springer 2011:5-14.
- 34. Ed. J Middleton GP, M L Jones. Computer methods in biomechanics and biomedical engineering 2: CRC Press; 1999. 126 p.
- 35. Pal S. Design of artifical human joints and organs: Springer; 2014.
- 36. Bilston LE, Thibault LE. The mechanical properties of the human cervical spinal cord in vitro. Ann Biomed Eng 1996;24:67-74.
- 37. Cai Z, Richards DG, Lenhardt ML, Madsen AG. Response of human skull to bone-conducted sound in the audiometric-ultrasonic range. Int Tinnitus J 2002;8(1):3-8.
- 38. Franke EK. The response of the human skull to mechanical vibrations. Ohio, USA: Wright-Patterson Air Force Base 1954.
- 39. Honarvar M, Sahebjavaher R, Sinkus R, Rohling R, Salcudean S. Curl-based Finite Element Reconstruction of the Shear Modulus Without Assuming Local Homogeneity: Time Harmonic Case. IEEE Trans Med Imaging 2013.
- 40. Fehlner A, Papazoglou S, McGarry MD, Paulsen KD, Guo J, Streitberger KJ, Hirsch S, Braun J, Sack I. Cerebral multifrequency MR elastography by remote excitation of intracranial shear waves. NMR Biomed 2015;28:1426-1432.

- 41. Johnson CL, Holtrop JL, McGarry MD, Weaver JB, Paulsen KD, Georgiadis JG, Sutton BP. 3D multislab, multishot acquisition for fast, whole-brain MR elastography with high signal-to-noise efficiency. Magn Reson Med 2014;71(2):477-485.
- 42. Sahebjavaher RS, Frew S, Bylinskii A, ter Beek L, Garteiser P, Honarvar M, Sinkus R, Salcudean S. Prostate MR elastography with transperineal electromagnetic actuation and a fast fractionally encoded steady-state gradient echo sequence. NMR Biomed 2014;27(7):784-794.
- 43. Feng Y, Abney TM, Okamoto RJ, Pless RB, Genin GM, Bayly PV. Relative brain displacement and deformation during constrained mild frontal head impact. J R Soc Interface 2010;7(53):1677-1688.
- 44. Clayton EH, Genin GM, Bayly PV. Transmission, attenuation and reflection of shear waves in the human brain. J R Soc Interface 2012;9(76):2899-2910.
- 45. Papazoglou S, Xu C, Hamhaber U, Siebert E, Bohner G, Klingebiel R, Braun J, Sack I. Scatter-based magnetic resonance elastography. Phys Med Biol 2009;54(7):2229-2241.
- 46. Romano A, Scheel M, Hirsch S, Braun J, Sack I. In vivo waveguide elastography of white matter tracts in the human brain. Magn Reson Med 2012;68(5):1410-1422.
- 47. Anderson AT, Johnson CL, Holtrop JL, Van Houten EE, McGarry MD, Paulsen KD, Sutton BP, Georgiadis JG. Property differences in white matter structures due to distinct wave propagation directions in MR elastography. Proc Int Soc Magn Reson Med 2015;23:1058.

Table 1 Simulation details

Simulation	NF/MRE	Model	No. of	Element	Boundary	Materials		
No.			Elements	volume	conditions			
					and loading			
1	NF	XM1	823001	≤ 2 mm ³	BC1	Cortical bone		
2	NF	XM1	823001	≤ 2 mm ³	BC2	Cortical bone		
3	NF	XM2	779408	≤ 2 mm³	BC1	Cortical bone		
4	NF	XM2	779408	≤ 2 mm ³	BC2	Cortical bone		
5	NF	XM3	838627	≤ 2 mm ³	BC1	Cortical bone		
6	NF	XM3	838627	≤ 2 mm³	BC3	Cortical bone		
7	NF	XM4	838627	≤ 2 mm ³	BC3	Cortical bone + cartilage #1		
8	NF	XM4	838627	≤ 2 mm³	BC3	Cortical bone + cartilage #2		
9	NF	XM5	838627	≤ 2 mm ³	BC3	Cortical + cancellous bone +		
						cartilage #2		
10	NF	XM5	838627	≤ 2 mm³	BC3	Viscoelastic cortical viscoelastic		
						cancellous bone + cartilage #2		
11	NF	XM6	1420763	≤ 4mm³	BC3+BC4	Viscoelastic cortical and cancellous		
				(brain, CSF		bone, cartilage #2, outer head,		
				and FTM ≤		brain, spinal cord, FTM, CSF		
				2 mm ³)				
12	NF	СТМ	712434	≤ 2 mm ³	BC3	Cortical bone		
13	MRE (5-	XM5	838627	≤ 2 mm ³	BC3+L1	Viscoelastic cortical bone +		
	150 Hz)					viscoelastic cancellous bone+		
						cartilage #2		
14	MRE (5-	XM5	838627	≤ 2 mm ³	BC3+L2	Viscoelastic cortical bone +		
	150 Hz)					viscoelastic cancellous bone+		
						cartilage #2		
15	MRE (5-	XM5	838627	≤ 2 mm ³	BC3+L3	Viscoelastic cortical bone +		
	150 Hz)					viscoelastic cancellous bone+		
						cartilage #2		
16	MRE (5-	XM5	838627	≤ 2 mm ³	BC3+L4	Viscoelastic cortical bone +		
	150 Hz)					viscoelastic cancellous bone+		
						cartilage #2		

17	MRE (5-	XM5	838627	≤ 2 mm ³	BC3+L5	Viscoelastic cortical bone +
	150 Hz)					viscoelastic cancellous bone+
						cartilage #2
18	MRE (5-	СТМ	712434	≤ 2 mm ³	BC3+L1	Cortical bone
	150 Hz)					
19	MRE (5-	СТМ	712434	≤ 2 mm ³	BC3+L2	Cortical bone
	150 Hz)					
20	MRE (5-	СТМ	712434	≤ 2 mm ³	BC3+L3	Cortical bone
	150 Hz)					
21	MRE (5-	СТМ	712434	≤ 2 mm ³	BC3+L4	Cortical bone
	150 Hz)					
22	MRE (5-	СТМ	712434	≤ 2 mm ³	BC3+L5	Cortical bone
	150 Hz)					
23	MRE (5-	XM6	1420763	≤ 4 mm ³	BC3+BC4+L1	Viscoelastic cortical and cancellous
	150 Hz)			(brain, CSF		bone, cartilage #2, outer head,
				and FTM ≤		brain, spinal cord, FTM, CSF
				2 mm ³)		
24	MRE (5-	XM6	1420763	≤ 4 mm ³	BC3+BC4+L2	Viscoelastic cortical and cancellous
	150 Hz)			(brain, CSF		bone, cartilage #2, outer head,
				and FTM ≤		brain, spinal cord, FTM, CSF
				2 mm ³)		
25	MRE (5-	XM6	1420763	≤ 4 mm³	BC3+BC4+L3	Viscoelastic cortical and cancellous
	150 Hz)			(brain, CSF		bone, cartilage #2, outer head,
				and FTM ≤		brain, spinal cord, FTM, CSF
				2 mm ³)		
26	MRE (5-	XM6	1420763	≤ 4 mm ³	BC3+BC4+L4	Viscoelastic cortical and cancellous
	150 Hz)			(brain, CSF		bone, cartilage #2, outer head,
				and FTM ≤		brain, spinal cord, FTM, CSF
				2 mm ³)		
27	MRE (5-	XM6	1420763	≤ 4 mm ³	BC3+BC4+L5	Viscoelastic cortical and cancellous
	150 Hz)			(brain, CSF		bone, cartilage #2, outer head,
				and FTM ≤		brain, spinal cord, FTM, CSF
				2 mm ³)		

Table 2: Constitutive parameter values employed in simulations

Tissue type	Parameter values										
	Young's modulus			Poisson's ratio			Density (kg/m³)				
	(MPa)										
Cortical bone	15,000			0.21			1,900				
Cancellous	4,600			0.05			1,500				
bone											
Cartilage #1	1			0.5				1,100			
Cartilage #2	1			0.1				1,100			
Outer head	16.7			0.42				1,000			
tissues											
Spinal cord	1.02			0.5			1,000				
FTM	31.5			0.45			1,130				
Brain	Frequency (Hz)		G' (Pa)		G'' (Pa)		1,000				
	25			1110		480					
	37.5			1310 570							
	50			1520		600					
	62.5			2010		800					
	90		3100		2500						
CSF	G ₀ (Pa)	G∞ (Pa)		β (s ⁻¹)		K (MPa)		1,000			
	1,000	900		80		1,050					
Viscous	t (s)	10		10 ²		10 ³		10 ⁴		10 ⁵	
damping	G(t)/G ₀	G(t)/G₀ 0.973		0.95		0.915		0.853		0.773	
cortical bone											
Viscous	t (s)	1	2	3	4	5	6	7	8	9	10
damping	G(t)/G ₀	0.93	0.9	0.888	0.873	0.865	0.875	0.852	0.834	0.74	0.7
cancellous bone											

Table 3: First six non-zero natural frequencies for simulations

Simulation details					Natural Frequencies (Hz)						
No.	. Model BC		Material Types	#1	#2	#3	#4	#5	#6		
1	XM1	BC1	Cortical bone	2747	3223	3733	3833	3998	4507		
2	XM1	BC2	Cortical bone	321	459	817	1488	2348	2628		
3	XM2	BC1	Cortical bone	341	846	1352	1837	2482	2726		
4	XM2	BC2	Cortical bone	288	348	449	707	875	1356		
5	XM3	BC1	Cortical bone	336	792	827	1350	1682	1839		
6	XM3	ВС3	Cortical bone	54	82	124	281	407	600		
7	XM4	ВС3	Cortical bone	54	82	124	275	402	598		
			+ cartilage #1								
8	8 XM4 BC3		Cortical bone	54	82	124	233	384	586		
			+ cartilage #2								
9	XM5 BC3		Cortical +	55	84	127	233	387	578		
			cancellous bone +								
			cartilage #2								
10	10 XM5 BC3		Viscoelastic cortical and	55	84	127	233	387	578		
			cancellous bone + cartilage								
			#2								
11	XM6	BC3+BC4	Viscoelastic cortical and	15.4	16.0	16.1	16.4	17.1	17.8		
			cancellous bone, cartilage #2,								
			outer head, brain, spinal								
			cord, FTM, CSF								
12	СТМ	BC3	Cortical bone	115	127	230	406	974	1087		

FIGURE LEGENDS

Figure 1: Models from XCAT phantom (an anatomical data set derived from imaging). The models are denotedXM, and contain varying anatomical components and material properties. XM1: upper skull, excluding jaw and neck; XM2: upper skull including jaw, but excluding neck; XM3: upper skull, plus jaw and neck. (XM1-XM3 were ascribed uniform material properties of cortical bone). XM4: a refinement of XM3, with extra structures at the connection points of the jaw with the skull, which were modeled as cartilage. XM5: a refinement of XM4 in which the upper skull and jaw included inner regions of cancellous bone. XM6: a refinement of XM5 adding: 1) brain; 2) cerebrospinal fluid (CSF) surrounding the brain to approximate the meninges; 3) ventricles, filled with CSF; 4) the processes of the *dura mater*, the *falx cerebri* and the *tentorium and falx cerebelli* membranes (denoted "FTM"); 5) a single volume for the outer head tissues (skin, muscle, fat, etc.); 6) the section of spinal cord on the inside of the neck. The nodes selected for the prescribed boundary conditions (BC) are also displayed (BC1: free vibration of all nodes). BC2: tethering of nodes at the base of the skull close to where the neck would connect; BC3: tethering of nodes at the base of the neck; BC4: tethering of nodes at the base surface of the outer head tissues.

Figure 2: a) The model derived from the population average of CT data from patients (CTM). b)-f) Loading (L) positions and directions displayed with XM3 model (derived from XCAT phantom and consisting of skull, jaw and neck, and uniform material properties set to cortical bone).. b) L1 or "head cradle", with temples vibrating in head-foot direction. c) L2 temples vibrating left-right in opposite directions. d) L3 temples vibrating left-right in same direction. e) L4 or "acoustic pillow", posterior of skull vibrating in anterior-posterior direction. f) L5 or "bite-bar", upper and lower jaw vibrating in left-right direction. g)-j) Motion of skull associated with the first four natural frequencies (NF) of XM4 (refinement of XM3 with connect points between skull and jaw modeled as cartilage) with boundary condition BC3: g) NF#1; h) NF#2; i) NF#3; j) NF#4.

Figure 3: Comparison of mean x, y and z displacement components and overall displacement magnitudes against frequency for skull-only models for different wave delivery methods (loading, L). XM5 is the model derived from XCAT phantom and consists of skull, jaw and neck, regions of cartilage and cancellous bone, while the CTM model is derived from the population average of CT data from patients and includes only cortical bone. a) XM5 L1; b) CTM L1; c) XM5 L2; d) CTM L2; e) XM5 L3; f) CTM L3; g) XM5 L4; h) CTM L4; i) XM5 L5; j) CTM L5.

Figure 4: MRE simulation nodal displacement magnitudes in the XM5 model (derived from XCAT phantom and consists of skull, jaw and neck, regions of cartilage and cancellous bone) far from resonance and at the resonance peaks for different wave delivery methods (loading, L, see Fig. 2) for a loading amplitude of 10 μ m: a) example frequencies far from resonance: L1 at 50 Hz, L2at 90 Hz,L3 at 90 Hz,L4, at 50 Hz, L5, at 30 Hz; b) example resonant frequencies: L1 at 125 Hz, L2 at 55 Hz, L3 at 55 Hz, L4 at 85 Hz, and L5 at 55 Hz and 115 Hz.

Figure 5: For XM6 model (full head model derived from XCAT phantom), comparison of skull and brain mean x, y and z displacement components and overall displacement magnitudes against frequency for different wave delivery methods (loading, L): a) L1; b) L2; c) L3; d) L4; e) L5; f) Comparison of mean displacement magnitudes for wave delivery methods for skull and brain.

Figure 6: Comparison of the real component of the displacement fields in x, y and z, and the magnitude of the curl, and inversion reconstructions of G' and G'' at 50 Hz and 90 Hz for different wave delivery options (loading, L). The displacement components are plotted on the same color scale of -0.03 to 0.03 mm for ready comparison between directions, methods and frequencies. However for $Re(u_y)$ of L1 at 90 Hz the displacements are also plotted on the more appropriate scale of 0 to 0.07 mm.

Figure 7: Comparison of mean G' and G" from inversions of MRE simulations in XM6 (full head model derived from XCAT phantom), and Mean absolute percentage difference with ground truth (MAPD) of G' and G" for full and eroded brain masks for different wave delivery methods (loading, L), and MAPDs of voxel-wise average of all five loading methods for G' and G". a) Mean G' for full brain mask against frequency, separate error bar plots for each loading method with standard deviation error bars, and plot comparing mean values for loading methods without error bars; b) Mean G" for full brain mask against frequency, separate error bar plots, and comparison plot; c) MAPD of G' for full brain mask for five ground truth frequencies used in material specification for brain tissue, error bar plots and comparison plot; d) MAPD of G" for full brain mask, error bar plots and comparison plot; e) G' MAPD for eroded brain mask, error bar plots and comparison plot; f) G" MAPD for eroded brain mask, error bar plots for voxel-wise average over loading methods of G' and G", for full and eroded brain volumes.